AIAA SciTech Forum
5-9 January 2015, Kissimmee, Florida
56th AIAA/ASCE/AHS/ASC Structures, Structural Dynamics, and Materials Conference

10.2514/6.2015-0952

Leading- and Trailing- Edge Reversal of a Cambered Airfoil for Stopped Rotors

Robert Niemiec[1], George Jacobellis[2], and Farhan Gandhi[3]
Rotorcraft, Adaptive and Morphing Structures (RAMS) Lab
Department of Mechanical, Aerospace, and Nuclear Engineering
Rensselaer Polytechnic Institute, Troy, NY, 12180

For helicopters in very high-speed flight there is interest in stopping the rotor and having it operate as a fixed-wing. However, with conventional airfoils, one half of the stopped rotor/wing would be in reverse flow. To overcome this challenge, this paper focuses on airfoil reversal, where the sharp trailing-edge morphs into the rounded leading-edge, and vice-versa. Extending on a previous study that reversed symmetric airfoils, the current paper presents a design methodology and solution for reversal of a cambered airfoil. Navier Stokes CFD simulation results show that rather than using straight links to approximate a reference airfoil profile, curved links that exactly represent the nose to mid-chord section reduce aerodynamic penalties considerably despite the "bumps" they produce over the trailing-edge region. The aerodynamic performance of a curved-link reversible NACA 23012 was seen to be close to that of the reference NACA 23012. A curved-link reversible NACA 4-digit airfoil, with the same thickness and camber as the Fairchild Reverse Velocity Rotor (RVR) airfoil performed significantly better, aerodynamically, than the RVR airfoil in reverse flow. The study examined actuator force requirement, and showed that both the magnitude and direction of the actuator force required to resist the aerodynamic loads vary depending on the airfoil angle of attack and the internal mechanism design.

I. Introduction

For rotorcraft to operate in very high speed cruise, slowing down of the main rotor is required to alleviate compressibility effects on the advancing blade tips. To keep the advancing tip Mach number within prescribed limits, the rotor is slowed to a greater degree with increasing flight speed. At the limit, the slowed rotor becomes the stopped rotor, as the rotor ceases to spin and functions as a fixed wing. In the past, stopped rotor designs, including Sikorsky's X-wing (Refs. 1, 2), and Boeing's Canard Rotor-Wing (CRW) concept (Refs. 3, 4) have been developed and tested. The Sikorsky S-72 X-wing used a circulation control system to produce cyclic lift, rather than cyclic pitch as conventional rotorcraft do. This was achieved through computer controlled valves routing pressurized air from the engines into the rotor blades, which was released from the leading and trailing edges as necessary. The Boeing X-50A Dragonfly used jets located at the tips of the main wing, causing it to rotate and allowing it to function as a two-bladed, high-solidity rotor. Each of these concepts had its own challenges, including the complexity of the circulation control system on the X-wing, and the poor performance of elliptical airfoils in both the helicopter as well as the fixed-wing mode in the CRW.

If, instead of elliptical airfoils, conventional airfoils were used in the rotor/wing, in the stopped configuration one half of the wing would experience fully reversed flow (going from the sharp trailing-edge to the blunt leading edge). This results in highly separated and turbulent flows, which in turn lead to very large drag. While the use of elliptical airfoils alleviates the issue of reverse flow (as the ellipse is symmetric about the mid-chord, and thus performs equally in forward and reverse flow), the performance in low-speed fight (rotor mode) is adversely affected.

A previous study by the authors (Ref. 5) explored the design of a reversible airfoil where the sharp trailing-edge morphed into a rounded leading-edge shape, while the leading-edge simultaneously morphed into the trailing edge shape. Using a NACA 0012 airfoil as a point of departure, Ref. 5 reported on the design of a kinematic system whereby the airfoil would reverse on application of a small chordwise actuation input, leading to prototype fabrication and operational demonstration (Fig. 1). In that study, the outer profile of the NACA 0012 airfoil was approximated in a piecewise linear manner and fabricated using straight rigid links. A computational fluid dynamics

[1] Graduate Research Assistant, AIAA Student Member
[2] Graduate Research Assistant, AIAA Student Member
[3] Rosalind and John J. Redfern Jr. '33 Professor of Aerospace Engineering, AIAA Associate Fellow

(CFD) analysis demonstrated that the reversible airfoil outperformed the elliptical airfoil in terms of the maximum lift-to-drag ratio.

The present study advances the work reported in Ref. 5 in three specific areas. First, the design approach was extended to apply to reversal of cambered airfoils. Second, with the straight outer profile links in Ref. 5 producing slope discontinuities in the aerodynamic profile which resulted in sharp changes in pressure and associated aerodynamic losses, the present study examines the use of curved outer profile links to reduce these losses. And third, the present study calculates internal loads dues to aerodynamic pressure to determine actuator force requirements and examines how design changes could minimize actuation force requirement.

II. Analysis and Design

The baseline cambered airfoil that was used in the design process was the NACA 23012 airfoil (Ref. 6). The leading 50% of the upper and lower surfaces of the NACA 23012 were each approximated using a set of 5 linear segments, as shown in Fig. 2. On the upper surface, the endpoints of the chain, P_{1U} and P_{6U}, are fixed and the intermediate points (P_{2U} through P_{5U}) all lie on the NACA 23012 profile, as well. The chordwise position, B_x, of these intermediate points is identified by minimizing the error function between the reference NACA 23012 profile and the linearly interpolated profile.

$$Minimize:\ E = \sum_{i=1}^{5} \int_{B_{x_i}}^{B_{x_{i+1}}} \left[N(x) - \frac{N\left(B_{x_{i+1}}\right) - N\left(B_{x_i}\right)}{B_{x_{i+1}} - B_{x_i}}\left(x - B_{x_i}\right) - N\left(B_{x_i}\right)\right] dx \quad \textbf{(1)}$$

where *N(x)* represents the exact profile of the NACA 23012 evaluated at *x.* To prevent the links from becoming too small, which would complicate the manufacture of the airfoil, a minimum value of 0.015*c* was imposed on the magnitude of $(x_{i+1} - x_i)$. A similar process is used to identify the control points on the leading 50% of the lower surface (P_{2L} through P_{5L}). The process described above is an improvement over Ref. 5 where the choice of the control points on the profile was ad hoc. The solution the above process yields (the coordinates of the profile control points on the upper and lower surfaces in the leading edge configuration) is presented in Table 1, and represented to scale in Fig. 2.

The linear segments, L_{1U},… L_{5U}, on the upper surface and L_{1L},… L_{5L}, on the lower surface are referred to as the profile links. To obtain the trailing edge configuration, the first link, L_{1U}, is rotated about P_{1U} until it intersects the reference NACA 23012's upper surface profile aft of mid-chord. This produces the point P'_{2U} (Fig. 3). The second link, L_{2U}, is similarly rotated about P'_{2U} and intersection with the reference airfoil's profile produces the point P'_{3U}. The process continues in this manner till the final link, L_{5U}, is rotated about P'_{5U} to obtain the point P'_{6U} on the chordline. The procedure is repeated for the lower surface. The coordinates of the profile control points on the surface in the trailing edge configuration are also tabulated in Table 1, and the trailing-edge profile is represented to scale in Fig. 3.

The airfoil morphing problem then reduces to that of moving the individual profile control points P_{kU} to P'_{kU} and P_{kL} to P'_{kL} (k=2–6), which in turn move the profile links. The system has a set of control links on a single actuation rod connecting to the profile control points, as shown on Fig. 4. Movement of the profile control points (P_{kU} to P'_{kU} and P_{kL} to P'_{kL}) is achieved through the control links by translation of the actuation rod in the chordwise direction through a prescribed distance. The control links are not set directly on the actuation rod but offset by some distance, a, as shown on Fig. 4

Figure 5 shows the motion of a single profile control point from known coordinates (B_x, B_y) in the leading-edge configuration, to known coordinates (b_x, b_y) in the trailing-edge configuration, achieved by the chordwise motion of the actuation rod by some distance, Δx. The control link length, d, its offset on the actuation rod, a, the offset of the actuation rod from the chordline, q, and the actuation stroke, Δx, are all design variables. If d_{x1} and d_{y1} represent the lengths of the control link resolved along the chord and thickness direction corresponding to Fig. 5a (leading-edge configuration), and d_{x2} and d_{y2} represent the resolved lengths corresponding to Fig. 5b (trailing-edge configuration), then the following expressions can be written:

$$d_{x1} = B_x - h \quad \textbf{(2)}$$

$$d_{x2} = b_x - X \quad \textbf{(3)}$$

$$d_{y1} = B_y - a - q \quad \textbf{(4)}$$

$$d_{y2} = b_y - a - q \quad \textbf{(5)}$$

$$X = h - \Delta x \quad \textbf{(6)}$$

where X and h are the distances from the offset to midchord in the trailing edge and leading edge modes, respectively. Further, since the link is rigid,

$$d_{x1}^2 + d_{y1}^2 = d_{x2}^2 + d_{y2}^2 \quad \textbf{(7)}$$

Manipulation of Eqs 2–7 yields:

$$\sqrt{d_{x1}^2 + \left(B_y - a - q\right)^2 - \left(b_y - a - q\right)^2} - b_x + B_x - \Delta x - d_{x1} = 0 \quad \textbf{(8)}$$

Eq. 8 has four variables, and by parametrically varying the actuation rod offset from the chord line, q, the actuation stroke, Δx, and d_{x1}, the control link offset on the control rod, a, can be calculated, and all other parameters can be determined thereafter. The process used is represented schematically in the flow chart in Fig. 6, but several constraints need to be applied to achieve a feasible solution. These are discussed below.

At no point can the actuation rod exist outside the airfoil's profile. This places a maximum limit on a and h. The limit on a is determined by the thickness and camber distribution of the airfoil, and h is dependent on q, with a maximum of h=0.495c at q=0. In addition, the control links cannot become horizontal in the trailing edge configuration, as this would prevent actuation and distort the outer profile. This implies that $\tan^{-1}(d_{y2}/d_{x2})$ must be greater than a prescribed minimum value. In this case, a minimum value of 10° was found to be sufficient to prevent distortion of the outer profile. The control link offset on the control rod, a, is assigned a minimum value, so that when a pin is inserted, it will not interfere with any of the other links or anything attached to the actuation rod. For a cambered airfoil, the constraints on the control link offsets may be impossible to satisfy, as the chord line may be too close to the lower surface to facilitate a minimum offset while remaining within the airfoil's outer profile. To accommodate this, q is allowed to vary, and is generally greater than zero for a positively cambered airfoil. Δx is also allowed to vary in this study, and the addition of these two new design variables (compared to the study in Ref. 8 on symmetric airfoils) tremendously opens up the design space. The limits on q are determined by the y-coordinates of the points chosen to approximate the profile. For each value of q, Δx is swept from 0.02c to 0.035c, and for each value of Δx in increments of 0.001c, d_{x1} is swept from $-\Delta x$ to $5\Delta x$.

Equation 8 is considered for each control link sequentially. For each link, d_{x1} is swept from $-\Delta x$ to $5\Delta x$. For each d_{x1}, Eq. 8 is solved for a. The remaining parameters are calculated from this solution and checked against the constraints. If no constraint is violated, the solution is kept, and the next link is considered. If a constraint is violated, d_{x1} is incremented by $0.05\Delta x$. If d_{x1} reaches its maximum value without a valid solution appearing for any single link, the entire solution is invalid, and Δx is incremented. If Δx reaches its maximum value, it is reset, and q is incremented. The solution procedure is depicted in Fig. 6. If q exceeds its maximum value before a valid solution is found, there is no valid solution within the design space, and the solver exits. This procedure was applied to the modified NACA 23012 defined by the coordinates in Table 1 (and shown in Figs. 2 and 3) to design the reversal mechanism displayed in Fig. 7. The lengths of the links and offsets can be found in Table 2 and Table 3.

III. Computational Fluid Dynamics

A. Symmetric Airfoils

With the straight outer profile links of the reversible airfoil, the airfoil contour is a piecewise linear approximation to the ideal reference airfoil. Reference 5 explained how this causes the flow to locally accelerate and then decelerate as it negotiates the slope discontinuity between adjacent linear sections. CFD results were presented showing that relative to the smoothly contoured reference airfoil, low pressure spikes and high pressure troughs were observed around points of slope discontinuity for the piecewise linear reversible airfoil. This phenomenon was strongest near the airfoil leading edge, especially on the suction surface, and receded downstream.

To alleviate these pressure anomalies and the associated aerodynamic penalties, the use of curved profile links was considered. In the leading-edge configuration, curved links were introduced between the profile control points to *exactly replicate* the profile of the reference airfoil from the nose to 50% chord. When the leading-edge morphs to the trailing-edge configuration, however, these curved links produce a series of small bumps since the region aft of

50% chord has lower curvature in the reference airfoil. It was, however, hypothesized that completely eliminating error in the profile geometry in the leading-edge region, while accepting some in the trailing-edge region, would prove to be more aerodynamically beneficial. To examine this, the Transonic Unsteady Rotor Navier-Stokes (TURNS) CFD code (Ref. 7) was used, in a manner similar to Ref. 5. A hyperbolic C grid containing 1200 grid points around the airfoil surface and 97 points normal to the surface was used. The normal spacing at the surface was such that the value of y+ at the surface was less than 1. A previous study by the authors (Ref. 5) has shown that such a grid is sufficient to accurately predict lift and drag coefficients.

Figure 8 shows the geometries of a reference NACA 0013 airfoil, a straight-link reversible airfoil (developed in Ref. 5) and a curved-link reversible airfoil of the type described in the paragraph above. The pressure distributions round the three airfoils are shown in Fig. 9. The simulation results in Fig. 9 correspond to a Mach 0.4, Re = 4.5 million, and an angle of attack of 7 deg. With regards to the nomenclature in the legend box, the straight-link reversible airfoil (taken from Ref. 5) used the NACA 0012 as the reference, but, on fabrication, the thickness of the links (see Fig. 1) increased the maximum thickness of the prototype to greater than 12%, and is therefore referred to as the "straight-link reversible 0012+." The maximum thickness of the prototype was close to 13% and so aerodynamic comparisons are made with the NACA 0013. Also presented on Fig. 8 is the pressure distribution for the curved-link reversible 0012+ airfoil. While the straight reversible airfoil clearly shows significant pressure spikes and troughs, discussed above, these are completely absent in the case of the curved link reversible airfoil from the airfoil nose to mid-chord (Figs. 9 and 10a). In fact, the pressure near the nose for the curved-link reversible airfoil is very similar to that of the reference NACA 0013 airfoil (Fig. 10a). In the trailing-edge region the curved-link reversible airfoil, due to the bumps, does show difference in pressure distribution compared to the NACA 0013 (Fig. 10b), but these differences are much smaller than those of the straight-link reversible airfoil near the leading-edge.

Figures 11 and 12 show the aerodynamic lift and drag coefficients of the three airfoils as a function of angle of attack, and Fig. 13 provides a comparison of the lift/drag ratio. The curved-link reversible airfoil shows higher lift coefficients than its straight-link counterpart, with a maximum lift coefficient much closer to that of the reference NACA 0013 (Fig. 11). Similarly, the drag coefficient of the curved-link reversible airfoil is significantly lower than its straight-link counterpart at moderate to high angles of attack (Fig. 12). Consequently, the maximum lift/drag of the curved-link reversible airfoil is substantially greater than the straight-link reversible airfoil (Fig. 13) and close to that of the NACA 0013. Perhaps more surprisingly, on Fig. 12 the drag coefficient of the curved link reversible airfoil at angles of attack greater than 9 deg is observed to be even lower than that of the reference NACA 0013. Figure 14 shows the flow field around the NACA 0013 airfoil and the curved-link reversible 0012+ at 14 deg angle of attack. The curved-link reversible airfoil is seen to have a smaller wake than the reference NACA 0013. It appears that the increased thickness on the rear half allows the flow to stay attached longer on the upper surface. Furthermore, the thicker, more rounded trailing-edge results causes the flow on the lower surface to turn upward, which also contributes to a smaller wake. Although results are presented at 14 deg angle of attack to most starkly emphasize the phenomena, the same was observed at a lower angle of attack (12 deg), albeit to a lesser degree.

B. Cambered Airfoils

The results above clearly demonstrate the benefits of using curved-link reversible airfoils that better represent the profile forward of mid-chord rather than straight-link reversible airfoils. This section examines the aerodynamic performance of curved-link reversible airfoils that have camber. Specifically, a curved-link reversible NACA 23012 is compared to an ideal NACA 23012 airfoil. The Fairchild Reverse Velocity Rotor airfoil (Ref. 8) is also included in the comparison (as a passive, fixed geometry airfoil with rounded leading and trailing edges, that is designed to perform well in reverse flow). Since the Reverse Velocity Rotor (RVR) airfoil has a different thickness and camber, a curved-link reversible version of a NACA 4-digit airfoil that has the same thickness (12%) and camber (2.5%) as the RVR airfoil, is also considered in the comparison. Although the maximum thickness of the Fairchild RVR airfoil is at 40% chord, compared to the 30% chord location for the curved-link reversible NACA 4-digit airfoil, this was considered to be more of an apples-to-apples comparison. Figure 15 shows the profiles of all the airfoils considered in the comparison.

Figures 16 and 17 show the lift and drag coefficients of the cambered airfoils considered, as a function of angle of attack, and Fig. 18 shows the lift/drag ratio. The data for the Fairchild RVR airfoil, obtained from Ref. 8, is for a Reynolds number of 1–2 million and Mach 0.4. The data for the reference NACA 23012 airfoil is obtained from C-81 tables, and the data for the reversible curved-link NACA 23012 and the reversible curved-link NACA 4-digit airfoils are obtained using the TURNS CFD code with the same grid parameters as the symmetric airfoil.

Comparing the curved-link reversible NACA 23012 to the baseline NACA 23012, between 5–12 deg angle of attack its lift coefficient is observed to be slightly lower and its drag coefficient is observed to be slightly higher. Consequently, the maximum L/D is lower by 21%. Comparing the lift coefficient of the curved-link reversible NACA 4-digit airfoil to the Fairchild RVR airfoil (Fig. 16), the lift coefficient of the reversible airfoil is seen to fall between the values attained by the RVR airfoil in forward and reverse mode at moderate angles of attack. However, the maximum lift coefficient of the curved-link reversible airfoil is the highest. The drag coefficient of the curved-link reversible NACA 4-digit airfoil is slightly higher than the RVR airfoil in forward mode but much lower than the RVR airfoil in reverse mode (Fig. 17). Consequently, the maximum lift/drag ratio of the curved-link reversible NACA 4-digit airfoil is lower than the RVR airfoil in forward mode by about 16%, but it substantially outperforms the RVR airfoil in reverse mode. Not only is the maximum L/D of the curved-link reversible 4-digit airfoil 68 compared to 59 for the RVR airfoil in reverse mode, but the L/D ratio has a much broader plateau while that for the RVR in reverse flow quickly drops off.

IV. Force Analysis

To properly design an actuation system, knowledge of the force required to hold the reversible airfoil in shape is needed. The actuator used in Ref. 5 is a very strong electromechanical motor, which was chosen due to lack of knowledge of how much force would be necessary to achieve actuation, and the links were very thick and heavy. To understand how the aerodynamic loads affect the actuator, information about the internal loads must be acquired. Knowing the nature of the internal loads will also allow the links to be sized to properly carry load.

To analyze the internal loads, the pressure distribution from Ref. 5 was applied to a reversible NACA0012 constructed from linear links. To simplify the analysis, the pressure distribution over each link was concentrated at the endpoints as follows (See Fig. 19)

$$F_1 = \frac{\int_0^{L_{link}} P(l)(L_{link} - l)dl}{L_{link}} \tag{9}$$

$$F_2 = \frac{\int_0^{L_{link}} P(l)ldl}{L_{link}} \tag{10}$$

The forces were calculated on each link sequentially, and oriented normal to the link. At each joint, where two profile links meet, the forces on each link were summed to acquire the total aerodynamic force applied at that node. Fig. 20 shows a free-body diagram for a single node in the leading edge.

Given C_{i+1}, the tensile load in the preceding link as per Fig. 20, the system is statically determinate, and the internal loads on each profile link and control link can be calculated through a force balance. For the i^{th} joint (i=4–1), in the leading edge,

$$D_i \cos(\theta_i) + C_i \cos(\alpha_i) = C_{i+1} \cos(\alpha_{i+1}) + F_x \tag{11}$$

$$-D_i \sin(\theta_i) + C_i \sin(\alpha_i) = C_{i+1} \sin(\alpha_{i+1}) - F_y \tag{12}$$

$$D_i = \frac{C_{i+1} \cos(\alpha_{i+1}) \sin(\alpha_i) - C_{i+1} \cos(\alpha_i) \sin(\alpha_{i+1}) + F_x \sin(\alpha_i) - F_y \cos(\alpha_i)}{\cos(\alpha_i) \sin(\theta_i) + \sin(\alpha_i) \cos(\theta_i)} \tag{13}$$

$$C_i = \frac{C_{i+1} \cos(\alpha_{i+1}) \sin(\theta_i) - C_{i+1} \cos(\theta_i) \sin(\alpha_{i+1}) + F_x \sin(\theta_i) - F_y \cos(\theta_i)}{\cos(\alpha_i) \sin(\theta_i) + \sin(\alpha_i) \cos(\theta_i)} \tag{14}$$

where the force C_5 must be obtained in a separate manner, depending on the mechanism used to create the leading and trailing edges. In this study, C_5 is determined by applying the pressure distribution as if there were a rigid link beyond L_4 extending to the nose, where it meets an identical link associated with the lower surface. A similar procedure is applied to the trailing edge, until equilibrium at each node is solved. To determine the chordwise load on the actuation rod, the horizontal components of the tensile forces in each control link are summed as vectors (Equation 15). This is the force the actuator needs to overcome to maintain the reversible airfoil's shape. The force needed from the actuator is the negative of this force.

$$F_{actuation} = -\sum_{i=2}^{5} D_{i,Lu}\cos(\theta_{i,Lu}) + D_{i,Ll}\cos(\theta_{i,Ll}) - D_{i,Tu}\cos(\zeta_{i,Tu}) - D_{i,Tl}\cos(\zeta_{i,Tl}) \quad \textbf{(15)}$$

where L refers to the leading edge, T to the trailing edge, u to the upper surface, and l to the lower surface, and a positive actuation force is oriented toward the leading edge. θ and ζ are defined as they appear in Fig. 21.

This force balance was carried out for a series of pressure distributions associated with increasing angle of attack and for various internal configurations. It was observed that the magnitude of the actuation force is heavily dependent on the pressure distribution (and hence angle of attack), and also the orientation of the control links in the trailing edge mode. As the control links become more horizontal in the trailing edge mode ($\zeta \to 0$), they are less able to carry the primarily vertical aerodynamic loads, and the links experience a great deal of stress as a result. Additionally, since the control link is nearly horizontal, nearly all of the tension is transferred to the actuation rod. As ζ grows larger, both the magnitude of tension in the control link (since the link is aligned more closely to the load vector) and the component of that tension carried by the actuation rod decrease greatly. The change in internal loading is shown in Fig. 22.

Due to the orientation of the control links, a positive pressure on the leading edge tends to cause the leading-edge region to collapse and reverse the airfoil. The actuator is therefore required to provide a force towards the leading edge to prevent deformation. Conversely, a positive pressure on the trailing edge will tend to cause the leading-edge region to thicken, requiring the actuator to provide a force towards the trailing-edge. At low angles of attack, the large suction peak on the upper surface of the leading edge overpowers the negative pressure over the trailing edge (for $\zeta_{max} > 15°$) and an actuator must provide a force toward the trailing edge to maintain the airfoil shape. It is seen in Fig. 24 that when stall occurs around 12°, there is a rapid change in actuation force requirement toward the nose of the airfoil associated with the disappearance of the suction peak at the leading-edge on the upper surface. This phenomenon is observed for all the designs examined (various values of ζ in Fig. 23).

V. Conclusions

This paper focuses on the design of a reversible cambered airfoil, whose rounded leading-edge changes to a sharp trailing-edge, and vice-versa. Expanding on a previous study that undertook a similar effort for symmetric airfoils, additional design parameters such as actuation rod offset from mean chord line are introduced, and the design space is further opened up by considering actuation stroke as a design parameter. The design process, and all the constraints, are outlined in detail, and a mechanism is presented that can reverse the NACA 23012 airfoil.

The previous study on reversal of symmetric airfoils, as well as the mechanism design process for cambered airfoil reversal in the present study, considered rigid, straight profile links to approximate the profile geometry of the reference airfoil. However, curved profile-links that exactly represent the nose to mid-chord sections can be used to avoid pressure spikes and troughs associated with slope discontinuities when straight profile links are used. Navier-Stokes CFD simulation results showed that the lift and drag coefficients of a reversible curved-link NACA 0012+ airfoil are closer to the reference airfoil than the reversible straight-link counterpart, despite "bumps" in the profile aft of mid-chord.

The aerodynamic performance of a reversible curved-link NACA 23012 was seen to be close to that of the reference NACA 23012 *airfoil*. Reversible airfoil comparisons were also made to a Fairchild Reverse Velocity Rotor (RVR) airfoil, with rounded leading- and trailing-edges. A reversible, curved-link NACA 4-digit airfoil with the same maximum thickness (12%) and camber (2.5%) as the RVR airfoil was used in the comparison (although the maximum thickness for the NACA 4-digit airfoil was at 30% chord and that for the RVR was at 40% chord). Although the aerodynamic performance of the reversible curved-link airfoil was a little lower than that of the RVR airfoil in forward mode, it substantially outperformed the RVR airfoil in reverse mode.

The aerodynamic pressure distribution on the rigid-link reversible airfoil was converted to forces on the profile control points, and the forces in the profile links, control links and the actuation rod were calculated. It was observed that the actuator force to prevent airfoil deformation under aerodynamic pressure varied in magnitude and

direction, depending on angle of attack and internal mechanism design. In future studies, the mechanism design can be adapted to minimize actuator force requirement, as best as possible.

REFERENCES

[1] Reader, K., and Wilkerson, J. "Circulation Control Applied to a High Speed Helicopter Rotor," from 32nd Annual National Forum of the American Helicopter Society, Washington, D.C., May 1976.

[2] Linden, A. W., "Fifty Years of Sikorsky High Speed Concepts," Proceedings of the American Helicopter Society 64th Annual Forum, Montreal, Canada, April 29 - May 1, 2008.

[3] John W. Rutherford, S.M. Bass and S.D. Larsen, "Canard Rotor/Wing: A Revolutionary High-Speed Rotorcraft Concept," AIAA 93-1175, AIAA/AHS/ASEE Aerospace Design Conference, Irvine, CA, Feb 16-19, 1993.

[4] Pandya, S., and Aftosmis, M. "Computation of External Aerodynamics for a Canard Rotor/Wing Aircraft." From 39th AIAA Aerospace Sciences Meeting and Exhibit. Reno, NV, Jan. 2001.

[5] Niemiec, R., Jacobellis, G., and Gandhi, F., "Reversible Airfoils for Stopped Rotors in High Speed Flight," *Smart Mater. Struct.* 23 (2014) 115013.

[6] I. Abbot and A. E. von Doenhoff, "Theory of Wing Sections, including a summary of airfoil data," Dover Publications, 1959.

[7] G. R. Srinivasan, J. D. Baeder, S. Obayashi and W. J. Mccroskey, "Flowfield of a lifting rotor in hover - A Navier-Stokes simulation," *AIAA Journal*, vol. 30, no. 10, pp. 2371-2378, Oct 1992.

[8] Ewans, J. & Krause, T., "Model Wind Tunnel Tests of a Reverse Velocity Rotor System", Technical report, Naval Air Systems Command, HC144R1070. 1973.

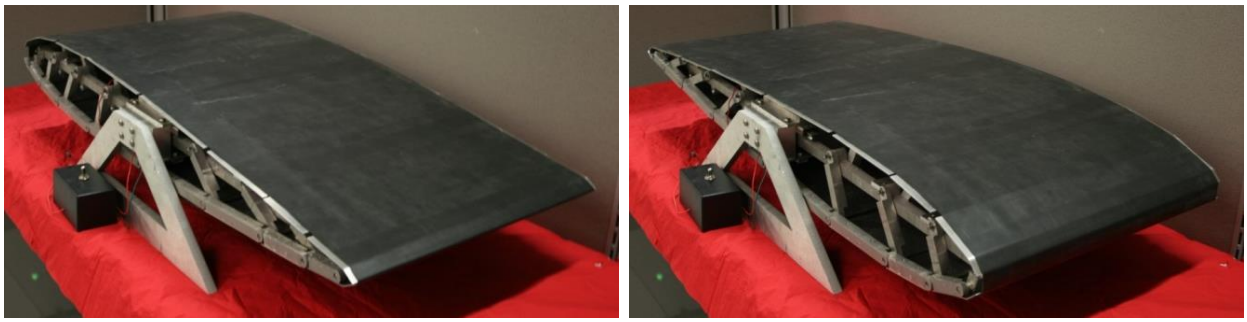

(a) (b)

Fig. 1. A reversible airfoil

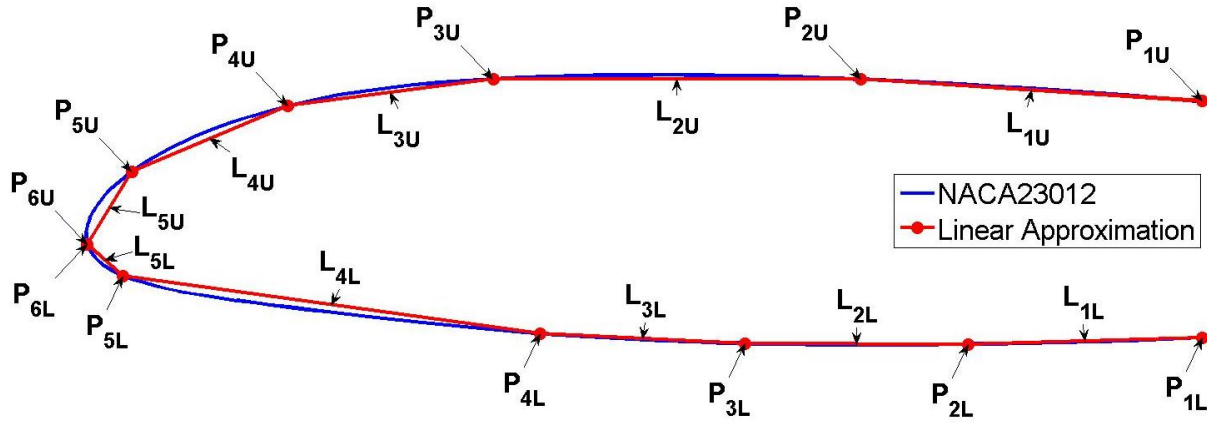

Fig. 2. The leading 50% of the NACA 23012 is approximated by 5 linear segments. The x-coordinates are chosen to minimize the area between the exact NACA 23012 profile and the linear approximation.

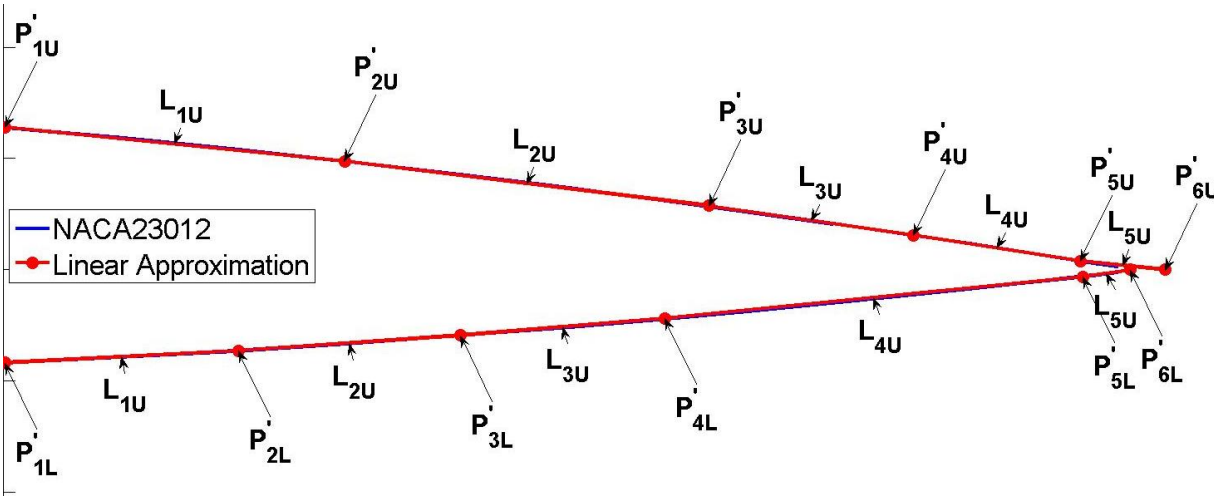

Fig. 3. The trailing 50% of the NACA 23012 is approximated by 5 linear segments.

Table 1. Coordinates of approximate NACA 23012

Upper Surface						Lower Surface					
Leading Edge			Trailing Edge			Leading Edge			Trailing Edge		
Point	B_x	B_y	Point	b_x	b_y	Point	B_x	B_y	Point	b_x	b_y
P_{1U}	0	0.0641	P'_{1U}	0	0.0641	P_{1L}	0	-0.0418	P'_{1L}	0	-0.0418
P_{2U}	0.153	0.074	P'_{2U}	0.1526	0.0489	P_{2L}	0.105	-0.0448	P'_{2L}	0.1049	-0.0364
P_{3U}	0.318	0.074	P'_{3U}	0.3163	0.0287	P_{3L}	0.205	-0.0444	P'_{3L}	0.2047	-0.0295
P_{4U}	0.410	0.062	P'_{4U}	0.4082	0.0155	P_{4L}	0.297	-0.04	P'_{4L}	0.2965	-0.0218
P_{5U}	0.480	0.0326	P'_{5U}	0.4832	0.0039	P_{5L}	0.484	-0.0141	P'_{5L}	0.4843	-0.0032
P_{6U}	0.5	0	P'_{6U}	0.5213	0	P_{6L}	0.5	0	P'_{6L}	0.5056	0

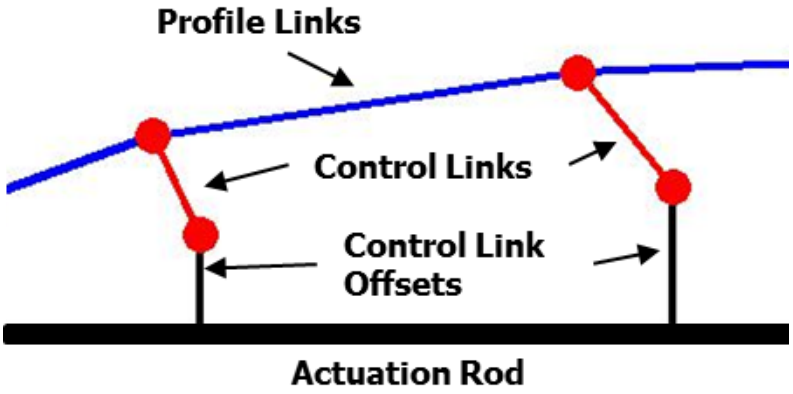

Fig. 4. Control links connecting profile link endpoints to actuation rod

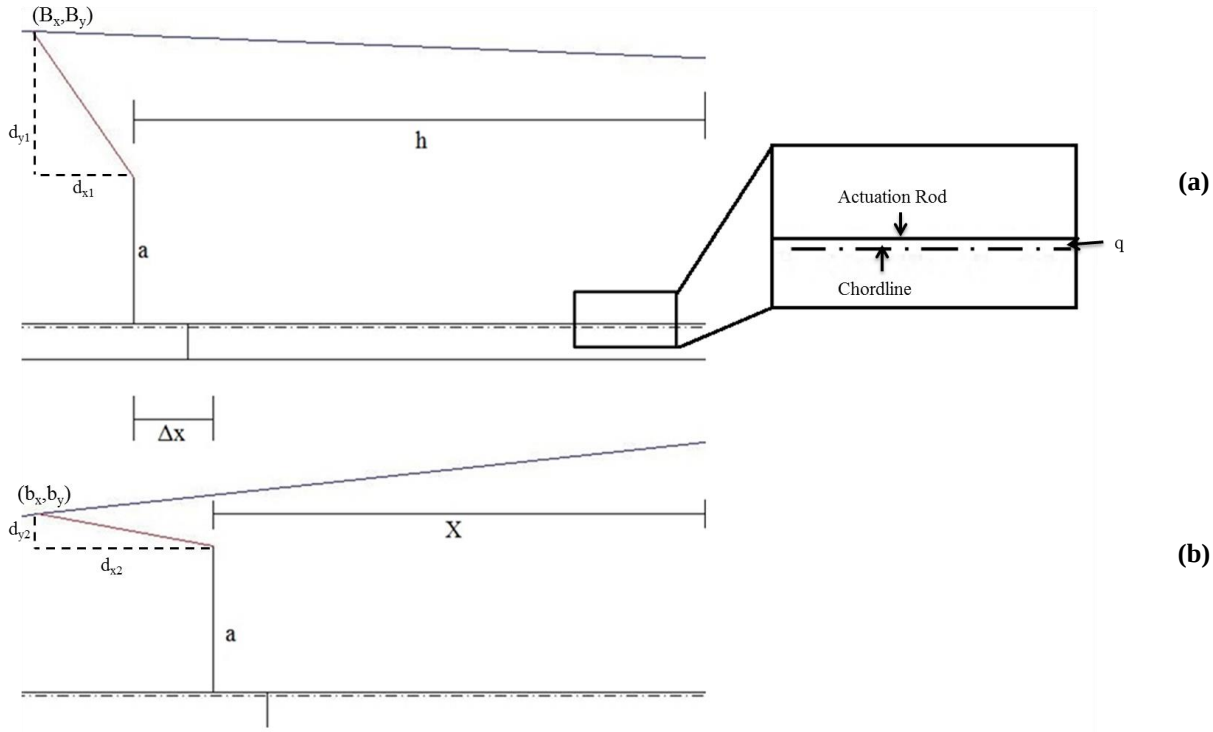

Fig. 5. Schematic of the reversible airfoil's mechanism (a) in the leading edge mode, (b) in the trailing edge mode

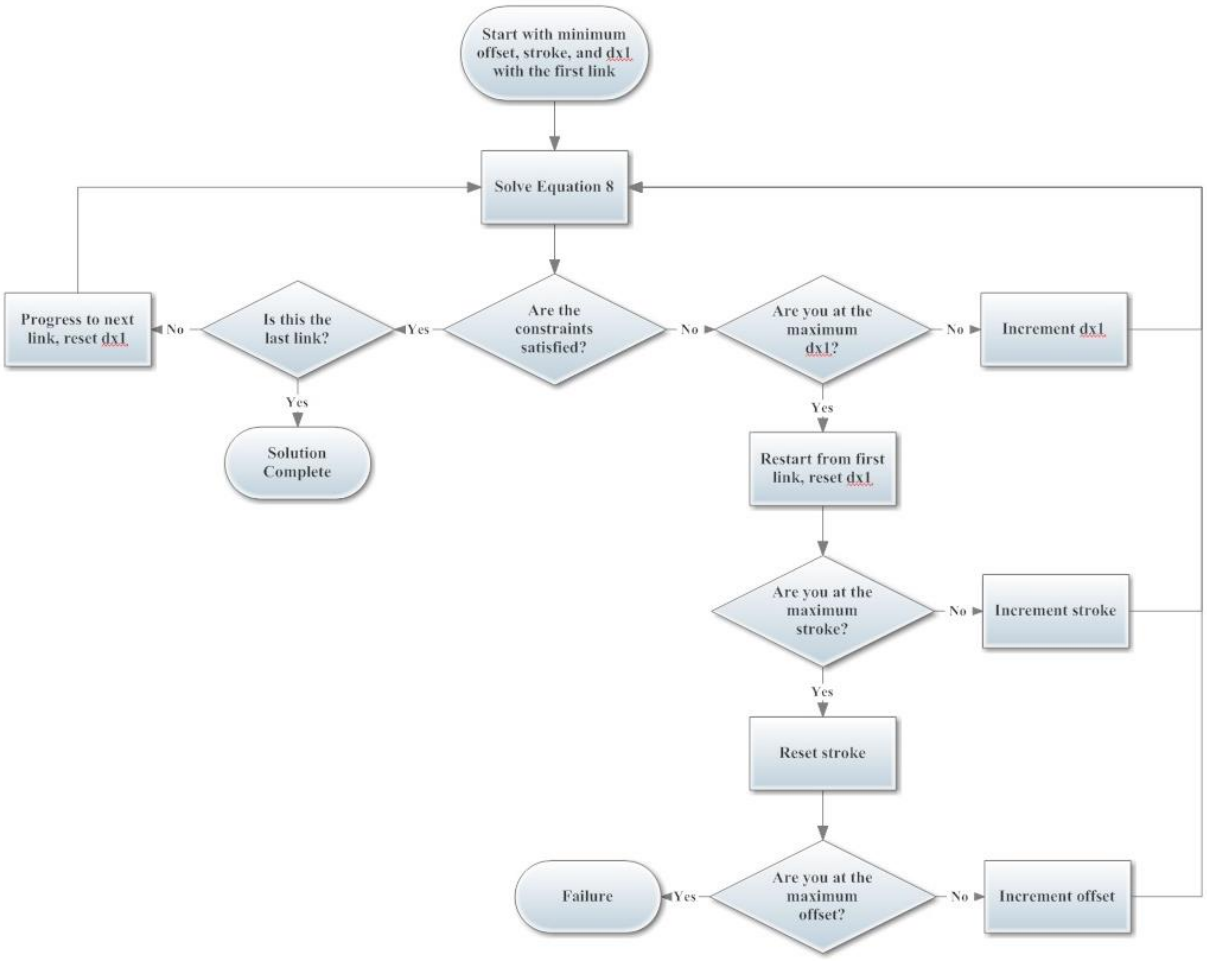

Fig. 6. Flowchart depicting the solution procedure taken to design a reversible airfoil

Table 2. Relative link lengths for upper surface of a reversible NACA 23012. Δx/c=0.03, q/c = 0

Profile Links		Control Links		Actuation Rod		
Number	Length/chord	Number	Length/chord	Number	Length/chord	Position/chord
1	0.1533	1	0.1170	1	-0.0265	0.0930
2	0.1650	2	0.1292	2	-0.0158	0.2250
3	0.0928	3	0.0975	3	-0.0098	0.3440
4	0.0759	4	0.0372	4	-0.0044	0.4770

Table 3. Relative link lengths for lower surface of a reversible NACA 23012. Δx/c=0.03, q/c=0

Profile Links		Control Links		Actuation Rod		
Number	Length/chord	Number	Length/chord	Number	Length/chord	Position/chord
1	0.1050	1	0.0316	1	-0.0141	0.1125
2	0.1000	2	0.0257	2	-0.0194	0.2110
3	0.0921	3	0.0261	3	-0.0143	0.3015
4	0.1888	4	0.0212	4	0.0042	0.4945

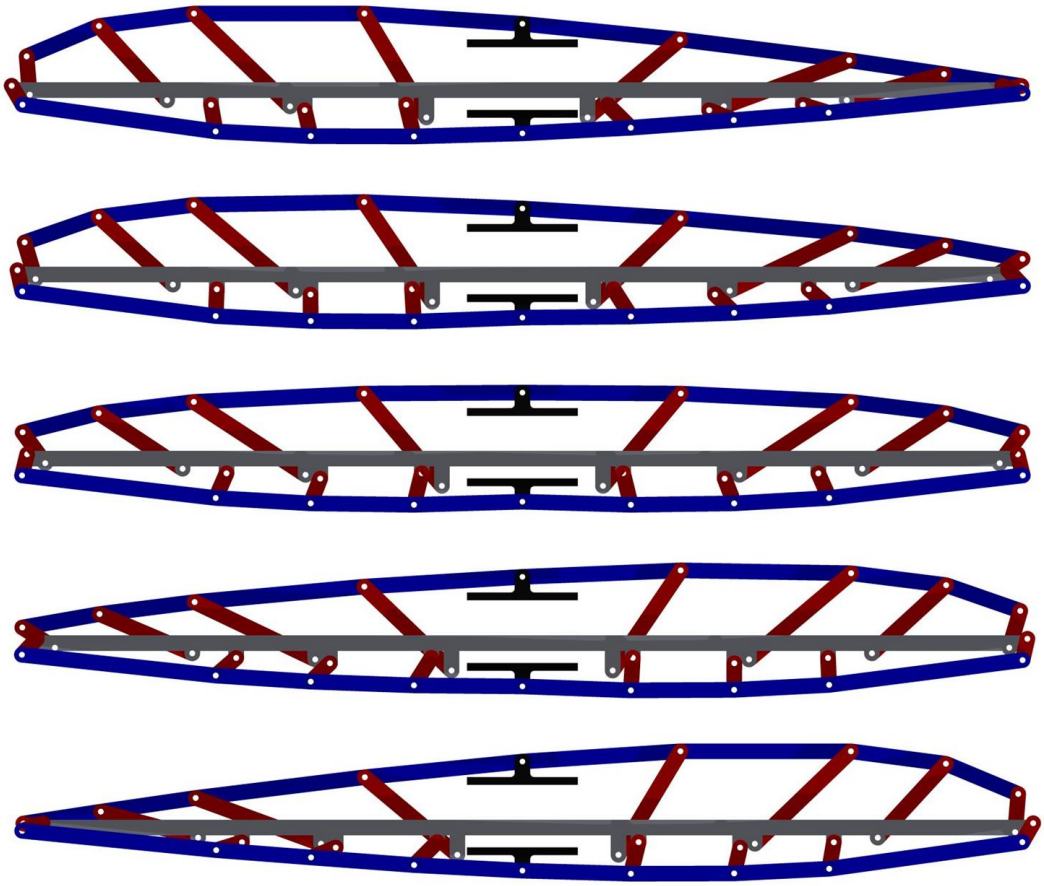

Fig. 7. Reversible NACA 23012

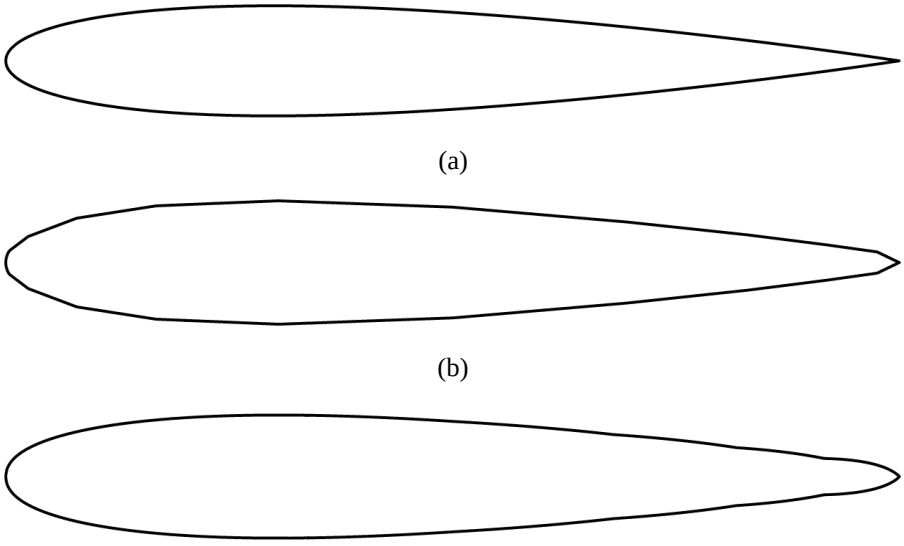

(a)

(b)

(c)

Fig. 8. Comparison of three airfoil profiles: (a) NACA 0013, (b) Straight link reversible NACA 0012+, (c) Curved-link reversible NACA 0012+

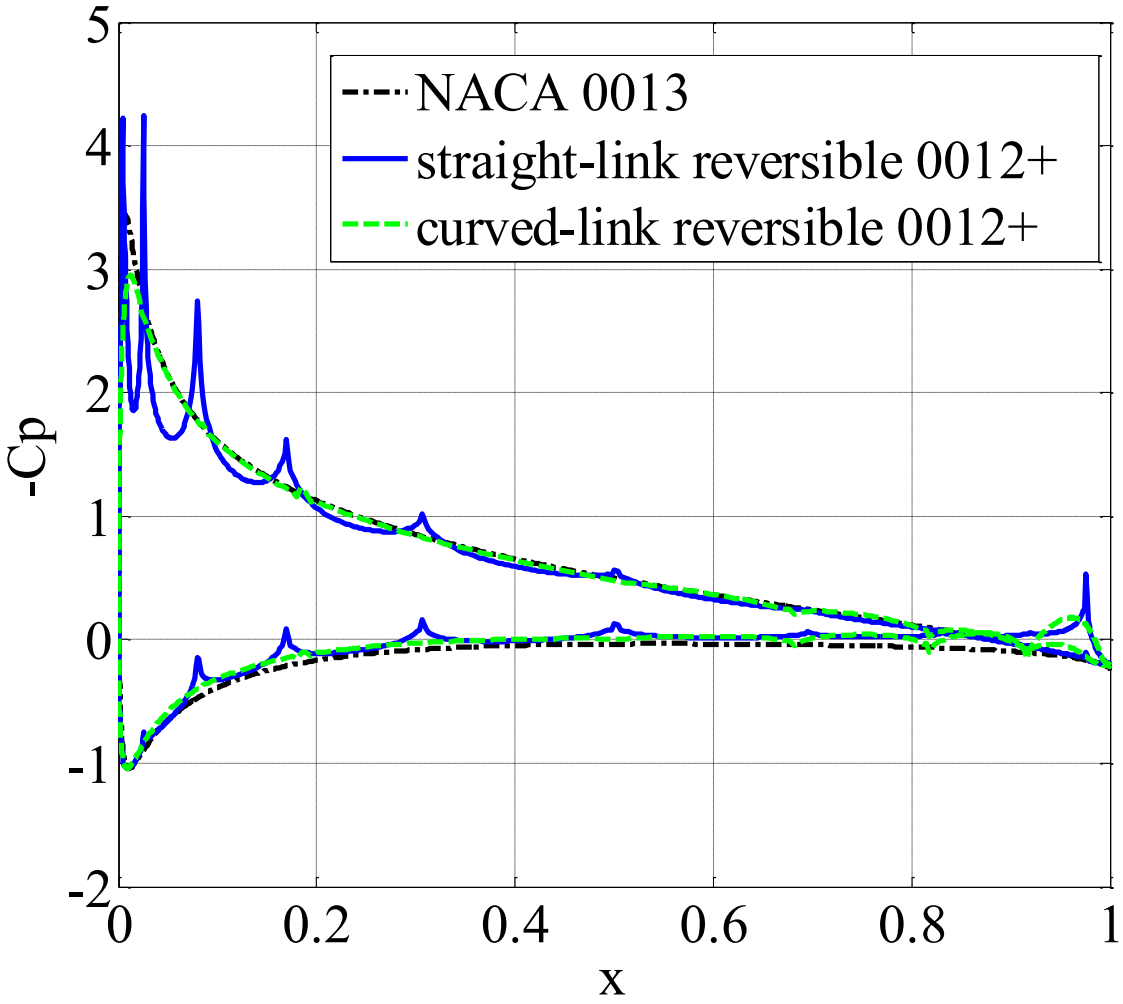

Fig. 9. Surface pressure coefficient on three symmetric airfoils at 7° angle of attack, Mach 0.4 Re=4.5million

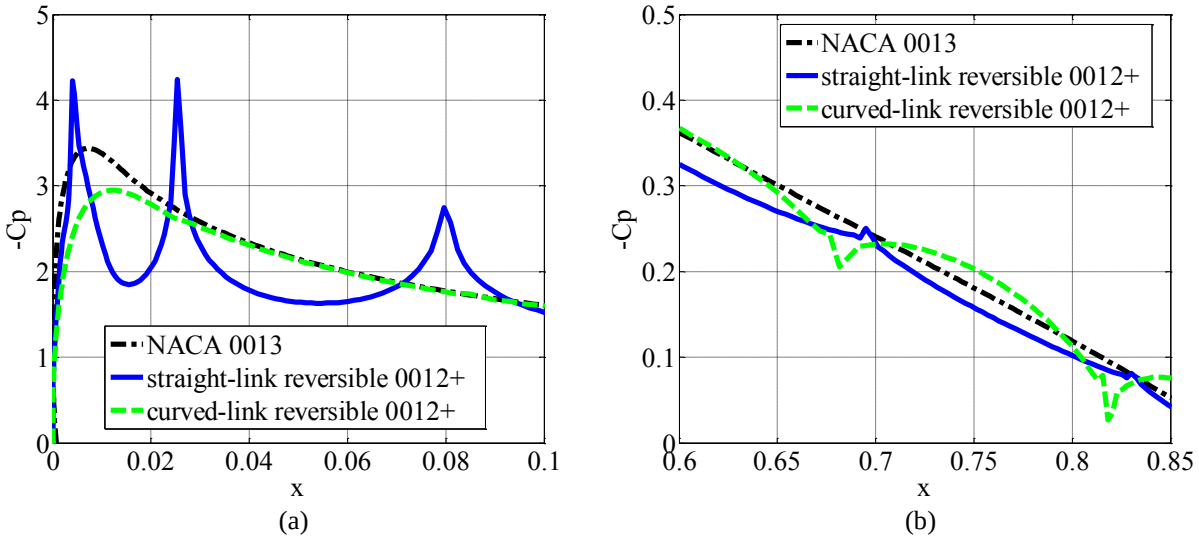

Fig. 10. Close-up of (a) leading edge surface pressure (b) trailing edge surface pressure

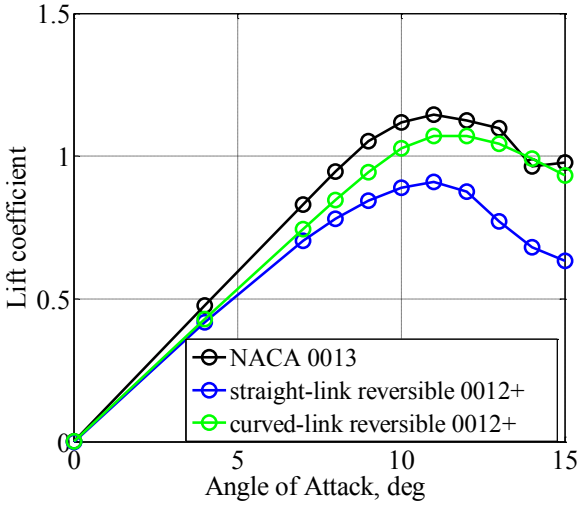

Fig. 11. Lift Coefficient symmetric airfoils at M=0.4

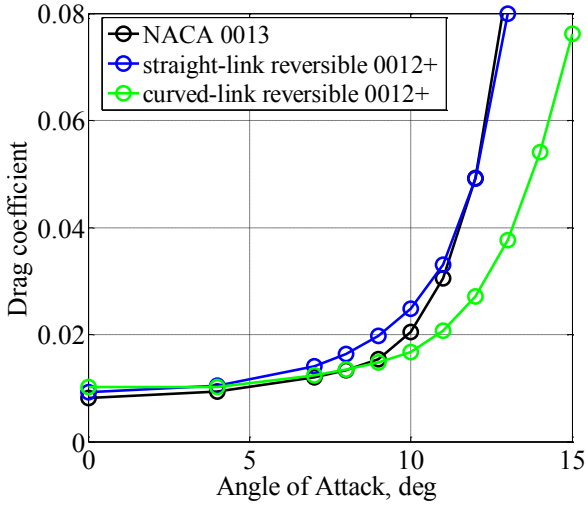

Fig. 12. Drag Coefficient symmetric airfoils at M=0.4

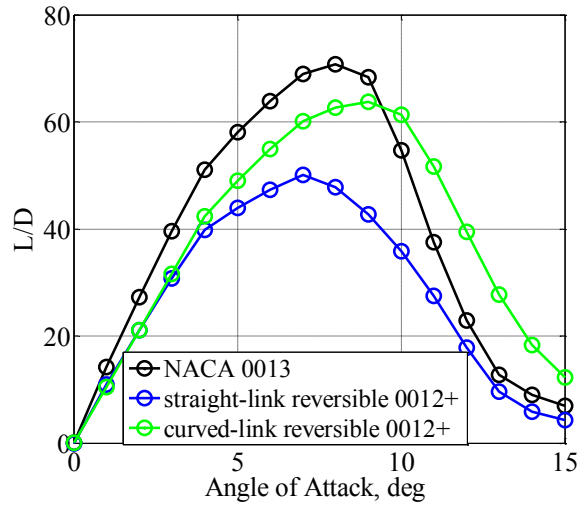

Fig. 13. Lift to drag ratio symmetric airfoils at M=0.4

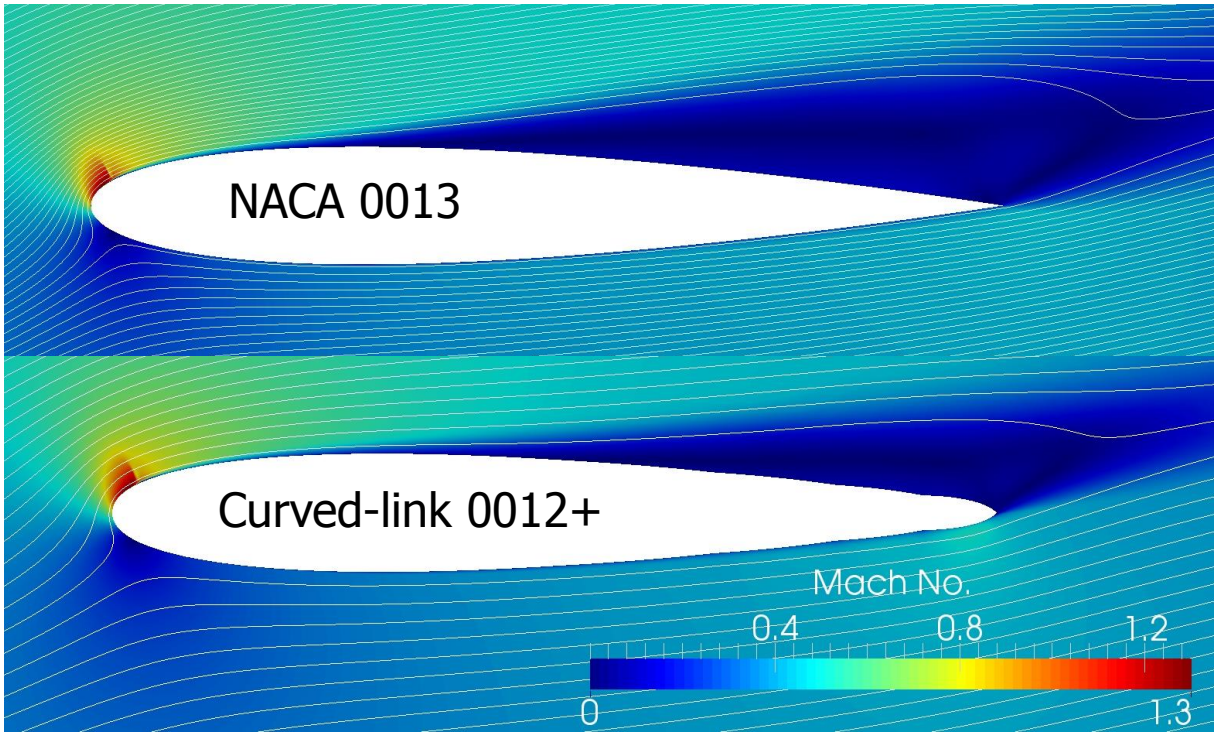

Fig. 14. Flow field around NACA 0013 (top) and curved-link reversible airfoil (bottom), at 14° angle of attack

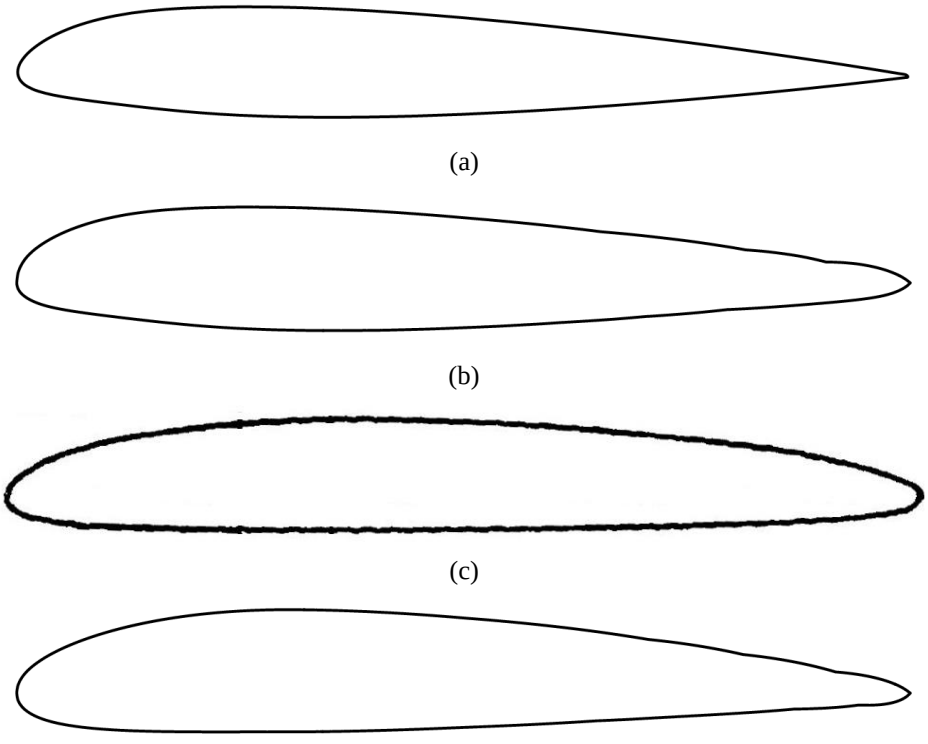

(a)

(b)

(c)

(d)

Fig. 15. Comparison of 4 cambered airfoil profiles: (a) NACA 23012, (b) curved link reversible NACA 23012, (c) Fairchild Reverse velocity rotor airfoil, (d) NACA 4-digit series reversible airfoil, 2.5% maximum camber at 30% chord

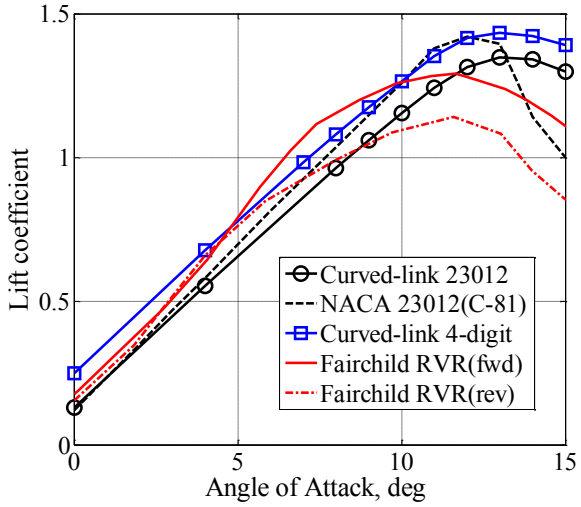

Fig. 16. Lift Coefficient on cambered airfoils at M=0.4

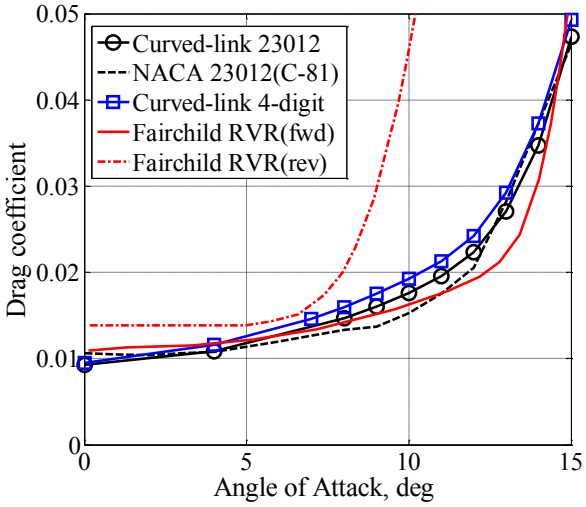

Fig. 17. Drag Coefficient on cambered airfoils at M=0.4

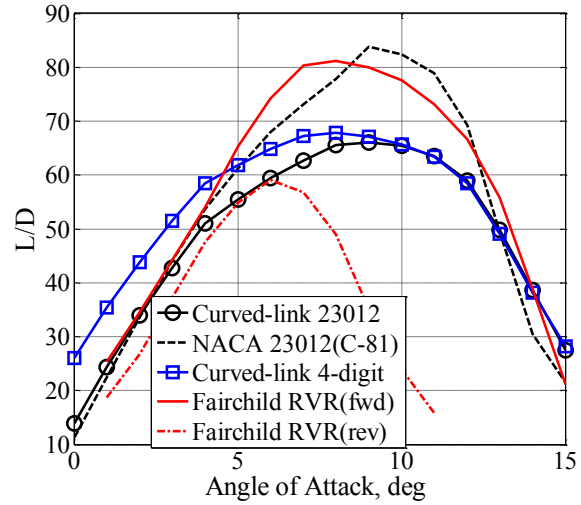

Fig 18. Lift to drag ratio of cambered airfoils at M=0.4

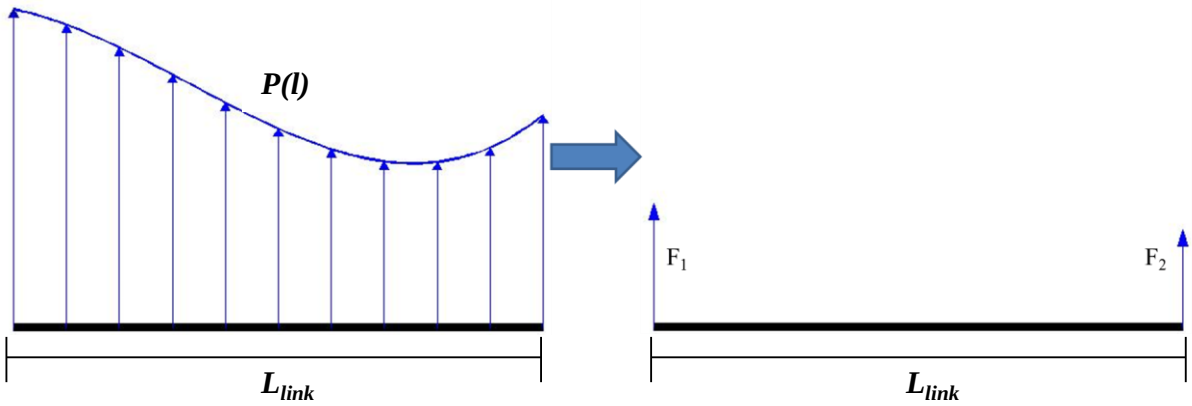

Fig. 19. A distributed load is concentrated on the endpoints

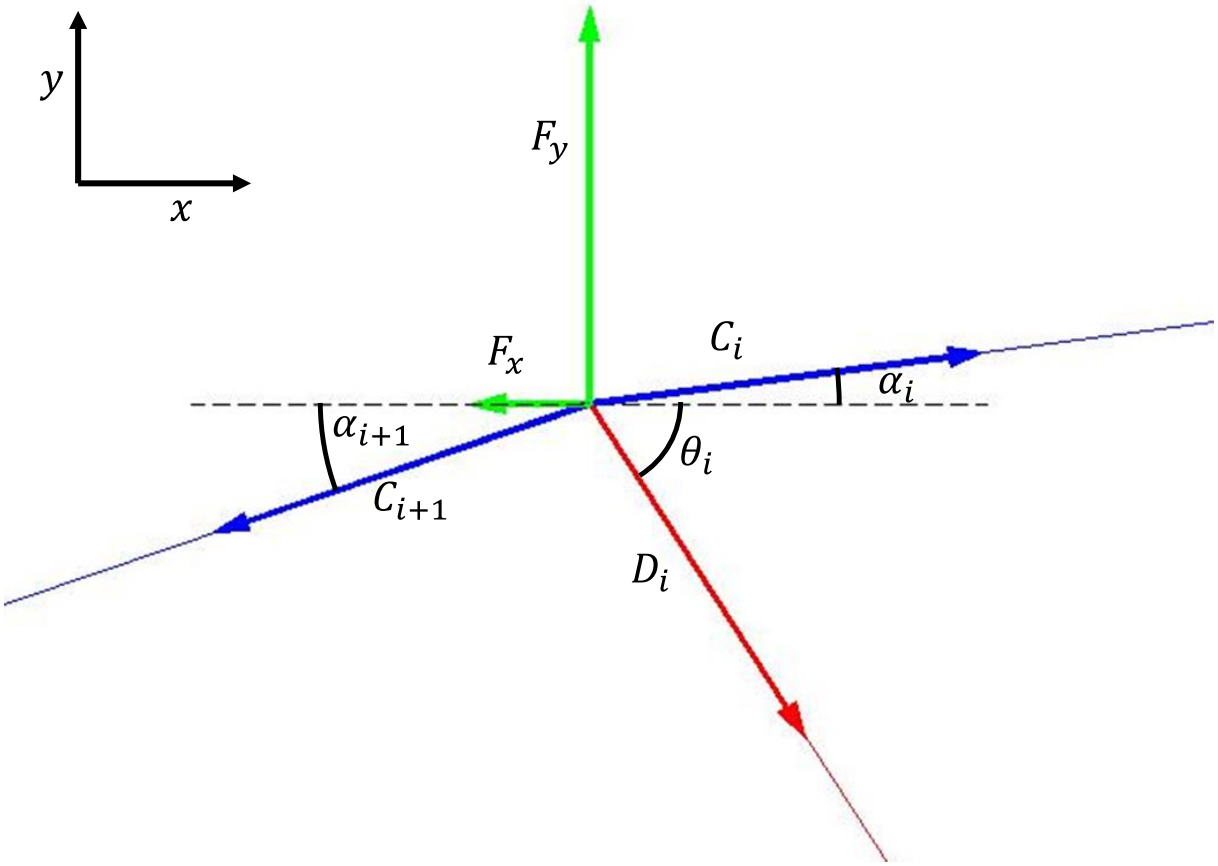

Fig. 20. Free-body diagram of a node in the leading edge. F_x and F_y are externally applied loads, C_i is a tensile load in the profile link, and D_i is a tensile load in the control link

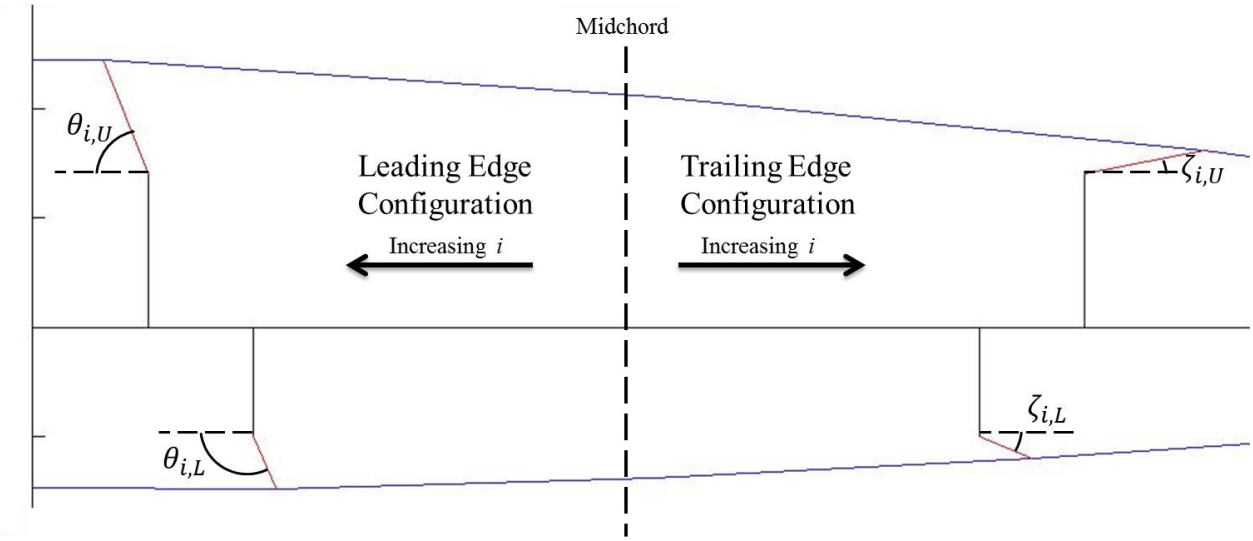

Fig. 21. Angle definition

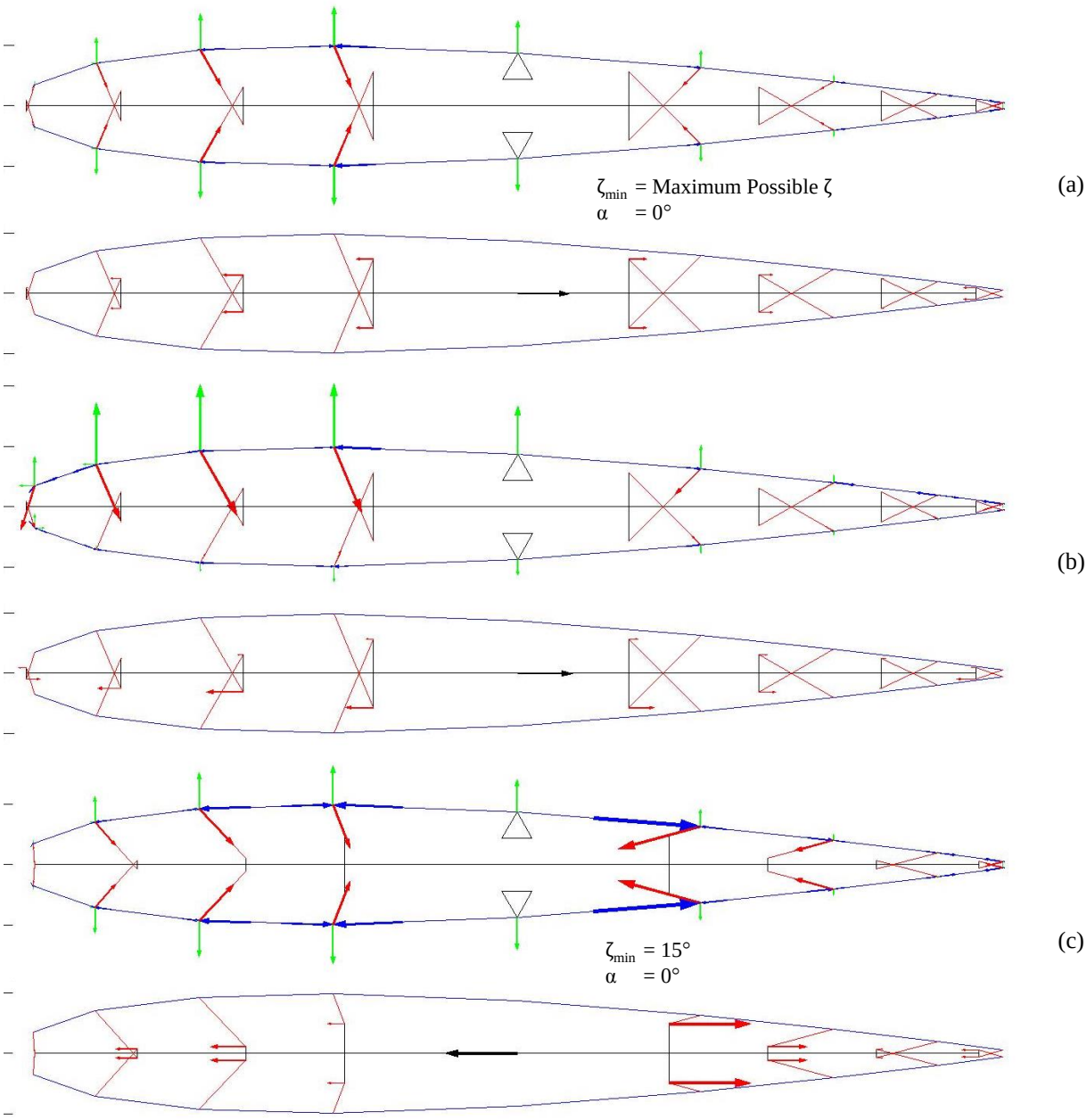

Fig. 22. The internal loading changes with angle of attack and control link configuration, (a) α=0° (b) α=4° (c) α=0°. The top airfoils show the tensile loads in the links in response to an aerodynamic load. The bottom airfoils show the actuation force required to maintain airfoil shape. As the control links become more horizontal in the trailing edge mode, the actuation force increases greatly

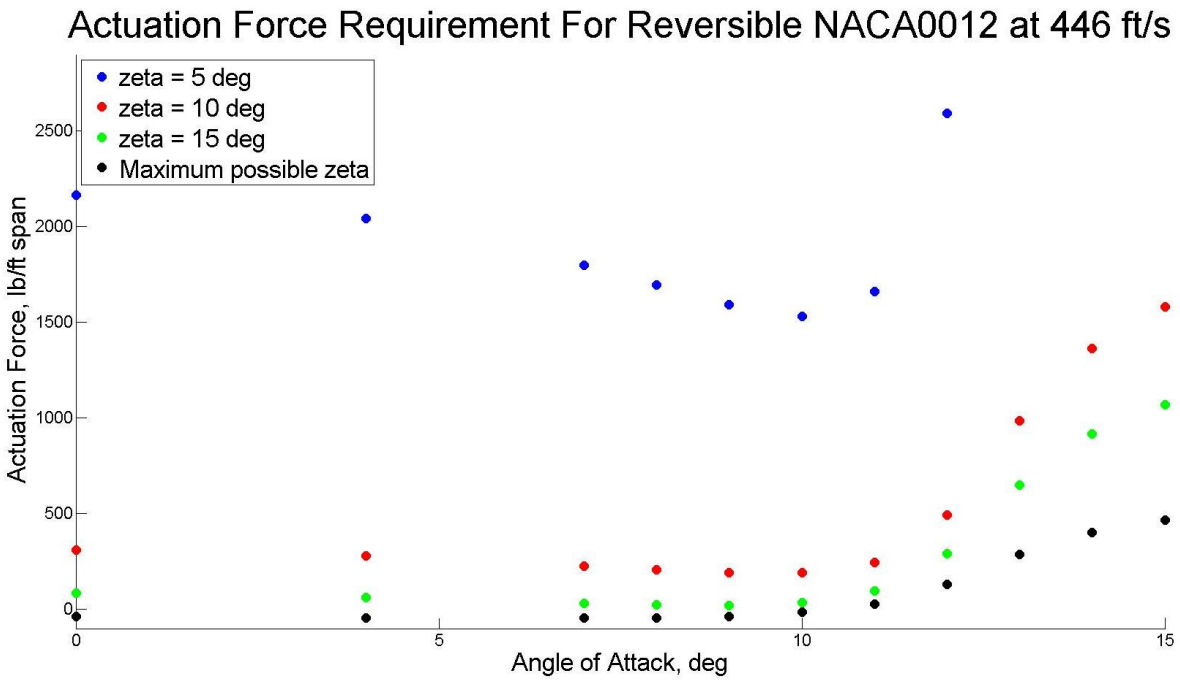

Fig. 23. Required actuation force is plotted against angle of attack for various values of ζ.